remote sensing

MDPI

Article

Performance Analysis of Ocean Surface Topography Altimetry by Ku-Band Near-Nadir Interferometric SAR

Weiya Kong [1,2,3], Jinsong Chong [1,2,*] and Hong Tan [4,5,*]

1 National Key Laboratory of Science and Technology on Microwave Imaging, Beijing 100190, China; kongweiya13@mails.ucas.ac.cn
2 Institute of Electronics, Chinese Academy of Sciences, Beijing 100190, China
3 School of Electronics, Electrical and Communication Engineering, University of Chinese Academy of Sciences, Beijing 100190, China
4 Technology and Engineering Center for Space Utilization, Chinese Academy of Sciences, Beijing 100094, China
5 Key Laboratory of Space Utilization, Chinese Academy of Sciences, Beijing 100094, China
* Correspondence: iecas_chong@163.com (J.C.); tanhong@csu.ac.cn (H.T.); Tel.: +86-10-5888-7125 (J.C.)

Received: 14 August 2017; Accepted: 6 September 2017; Published: 9 September 2017

Abstract: Interferometric imaging radar altimeter (InIRA) is the first spaceborne Ku-band interferometric synthetic aperture radar (InSAR) which is specially designed for ocean surface topography altimetry. It is on the Tiangong II space laboratory, which was launched on 15 September 2016. Different from any other spaceborne synthetic aperture radar (SAR), InIRA chooses a near-nadir incidence of 1°~8° in order to increase the altimetric precision and swath width. Limited by the size of the Tiangong II capsule, the baseline length of InIRA is only 2.3 m. However, benefitting from the low orbit, the signal-to-noise ratio of InIRA-acquired data is above 10 dB in most of the swath, which, to a certain extent, compensates for the short baseline deficiency. The altimetric precision is simulated based on the system parameters of InIRA. Results show that it is better than 7 cm on a 5-km grid and improves to 3 cm on a 10-km grid when the incidence is below 7.4°. The interferometric data of InIRA are processed to estimate the altimetric precision after a series of procedures (including image coregistration, flat-earth-phase removal, system parameters calibration and phase noise suppression). Results show that the estimated altimetric precision is close to but lower than the simulated precision among most of the swath. The intensity boundary phenomenon is first found between the near range and far range of the SAR images of InIRA. It can be explained by the modulation of ocean internal waves or oil slick, which smooths ocean surface roughness and causes the modulated area to appear either brighter or darker than its surroundings. This intensity boundary phenomenon indicates that the available swath of high altimetric precision will be narrower than expected.

Keywords: InSAR; near-nadir incidence; Ku-band; ocean surface topography; altimetry

1. Introduction

Under the influence of ocean tides, eddies and bathymetry variety, ocean surface topography (OST) changes at a global level [1,2]. Satellite radar altimetry has been utilized for over three decades since the first spaceborne radar altimeter on geodetic satellite (GEOSAT)to acquire high precision OST. Now the latest Poseidon-3B on Jason-3 can achieve a 2-cm precision [3]. The altimeter sends special shaped pulse to the nadir point and times the round trip delay to measure the ocean surface height. The pulse size projected on the ocean surface, also referred to as a footprint, decides the swath width and resolution of the altimeter, which is usually on the order of 2~10 km [4], as shown in Figure 1. An altimeter is none-imaging radar, it only measures one-dimensional OST along the satellite track.

It is difficult for an altimeter to map mesoscale or sub-mesoscale (15~300 km) oceanic processes, since a 200~300 km gap usually exists between two successive tracks. Therefore, an altimeter is normally used to study large-scale (>300 km) oceanic processes [5].

In recent years, there has been a growing demand for scientific research on mesoscale and sub-mesoscale oceanic processes, such as eddies and currents [6,7]. Interferometric synthetic aperture radar (InSAR), which is capable of measuring OST with high precision and a wide swath, is expected to be the next generation of satellite altimeter. InSAR has been successfully used to map terrain elevation, and the Shuttle Radar Topography Mission (SRTM) is one of the most typical examples [8]. InSAR altimetry is performed by acquiring two synthetic aperture radar (SAR) complex images of the same region during the single pass or repeat pass of the satellite [9]. Topography change is then recorded by the interferometric phase, which is the phase difference between two SAR complex images [10]. Different from terrain elevation measurement, ocean surface height changes randomly, hence two SAR antennas should be borne on satellites to acquire the images simultaneously. Moreover, OST altimetry demands centimeter-level precision, which is far beyond the capability of current InSAR systems. Therefore, several key parameters of InSAR need to be adjusted to fulfill the stringent requirements, which include near-nadir incidence, long physical baseline and short radar wavelength, and near-nadir incidence is the most distinctive characteristic from any other existing InSAR systems. Near-nadir InSAR is imaging radar; by using a pulse compressing technique, the image resolution is about a few meters, which is much smaller than its swath, as shown in Figure 1. Therefore, near-nadir InSAR can be used to measure surface water (lakes, rivers, wetlands, etc.) as well [11].

The wide-swath ocean altimeter (WSOA) is the first near-nadir InSAR proposed by National Aeronautics and Space Administration (NASA), and its two antennas work at Ku-band and form a baseline of 6.4 m. The incidence ranges from 0.6° to 4°, and a 5-cm precision is expected on a 15 km grid [12,13]. However, due to the technical limitations at that time, WSOA was finally canceled. The Surface Water and Ocean Topography (SWOT) mission, a collaboration between NASA and Centre National d'Etudes Spatiales (CNES), draws from the heritage of WSOA. KaRIN, as its main instrument, is a Ka-band near-nadir InSAR. A 10-m boom links its antennas to guarantee that the baseline is long enough to achieve a 3-cm precision on a 1-km grid. SWOT is planned to be launched in 2021 [5]. CNES carried out a series of airborne near-nadir InSAR experiments on surface water measurement to imitate SWOT performance [14,15]. Roger Fjørtoft [16] reported that the surface water was severely influenced by layover effect from its surrounding landscape because of the near-nadir incidence. Nevertheless, due to high land/water contrast, which was about 10~20 dB, the layover could be mitigated to some extent. Elizabeth H. Altenau et al. [17] used AirSWOT (an airborne near-nadir InSAR which was developed by Jet Propulsion Laboratory) collected near-nadir InSAR data to retrieve water surface elevation of the Tanana River, Alaska. Verified by in situ measurements, results showed that the root-mean-square error (RMSE) was 9 cm for water surface elevation averaged over 1-km^2 areas.

The interferometric imaging radar altimeter (InIRA), as an experimental payload, was developed by the National Space Science Center, Chinese Academy of Sciences. InIRA is borne on Tiangong II, the Chinese space laboratory, which was launched on 15 September 2016 and runs in a non-sun-synchronous orbit at an altitude of about 400 km. InIRA is the second spaceborne InSAR that can perform single-pass interferometry after SRTM. Its two antennas work at Ku-band and form a baseline of 2.3 m. As shown in Figure 1, due to the wide range of the incidence (1°~8°), a swath larger than 40 km can be achieved along the right side of the orbit track. The usual SAR incidence varies from 20° to 60°, which determines that Bragg scattering is prevalent among the received signal [18]. While under the near-nadir incidence, specular-reflected signal from ocean surface dominates, which makes InIRA acquired data quite unique from any other SAR images.

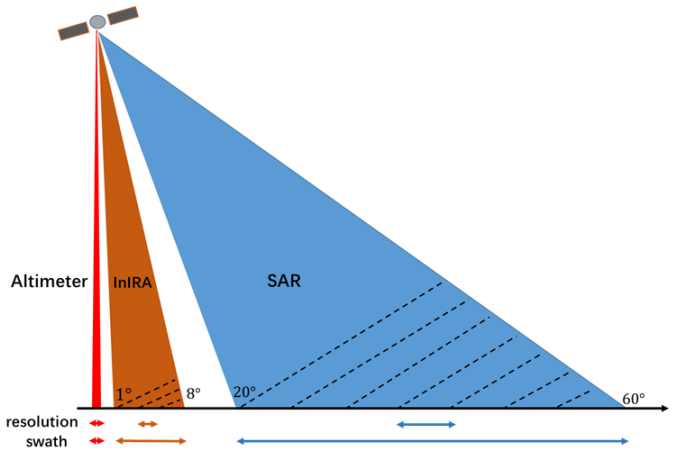

Figure 1. Schematic diagram of the resolution and swath of an altimeter, interferometric imaging radar altimeter (InIRA) and synthetic aperture radar (SAR) (the sketch does not represent the actual geometrical size).

In this paper, we analyze the performance of InIRA on ocean surface topography altimetry to evaluate its capabilities on exploiting various oceanic processes; in Section 2, the measurement principle of near-nadir InSAR is briefly introduced and the altimetric precision is simulated based on the system parameters of InIRA; in Section 3, after a series of data processing procedures, the altimetric precision on a 1-km grid is estimated from the multi-look interferometric phase; in Section 4, the intensity boundary phenomenon of near-nadir InSAR image is first found and discussed; some recommendations of parameter design for future near-nadir InSAR are given based on the performance of InIRA in Section 5.

2. Altimetry Simulation of OST

2.1. System Parameters of InIRA

All system parameters of InIRA are designed in order to increase its altimetric precision and swath width; however, limited by the capsule size of Tiangong II and the compatible requirements with other experiment payloads, some of the system parameters are restricted.

The altimetric precision of InSAR is given by [10]:

$$\Delta h = \frac{\lambda r_1 \sin\theta}{2\pi B \cos(\theta - \alpha)} \Delta\phi \tag{1}$$

where B is the physical baseline length, λ is the radar wavelength, θ is the incidence, α is the baseline roll angle, and $\Delta\phi$ is the phase error. Therefore, a longer baseline, smaller incidence and shorter radar wavelength will improve the altimetric precision significantly.

The antennas are installed outside the capsule of Tiangong II and form a 2.3-m baseline. The baseline length is quite short for the high altimetric precision requirement. In order to compensate for the short baseline deficiency, a near-nadir incidence is chosen. A bonus brought by the near-nadir incidence is that the received signals are mainly from specular reflection, which improves the signal-to-noise ratio (SNR) a lot and further increases the altimetric precision. The relationship between SNR and altimetric precision is explained in Section 2.3.

Theoretically, the shorter the radar wavelength the higher the altimetric precision. However, short radar wavelength has its drawbacks, and rain attenuation will decrease the SNR of reflected signal and eventually worsen the altimetric precision [19]. Moreover, when an electromagnetic wave intersects with the ocean surface, short radar wavelength will lower the possibility of specular reflection because less surface appears smooth [16]. This will definitely worsen the precision as well since most of

the reflected signals come from specular reflection under near-nadir incidence. Hence, the Ku-band antennas are chosen for InIRA above all these considerations.

In order to achieve a wide swath, the relative variation of the incidence is quite large. The nominal incidence of InIRA is 1°~8°, as shown in Figure 2a; a 47-km-wide swath can be achieved within the incidence range, while a large relative variation of incidence also makes the ground-range resolution of InIRA change significantly. The ground-range resolution has changed almost eight times from ~213 m in the near range to ~27 m in the far range, as shown in Figure 2b.The variation of ground-range resolution also causes the multi-look number varies significantly among the swath. Averaging N neighboring pixels, also referred to as multi-looking, is normally used to reduce the phase error while processing the interferometric data [20]. The multi-look number is determined by the ratio between grid resolution and ground-range resolution. Supposing that the grid resolution along the ground-range direction is 1 km after multi-looking, then the phase error suppression by multi-looking in the near range of the swath will be much less than in the far range.

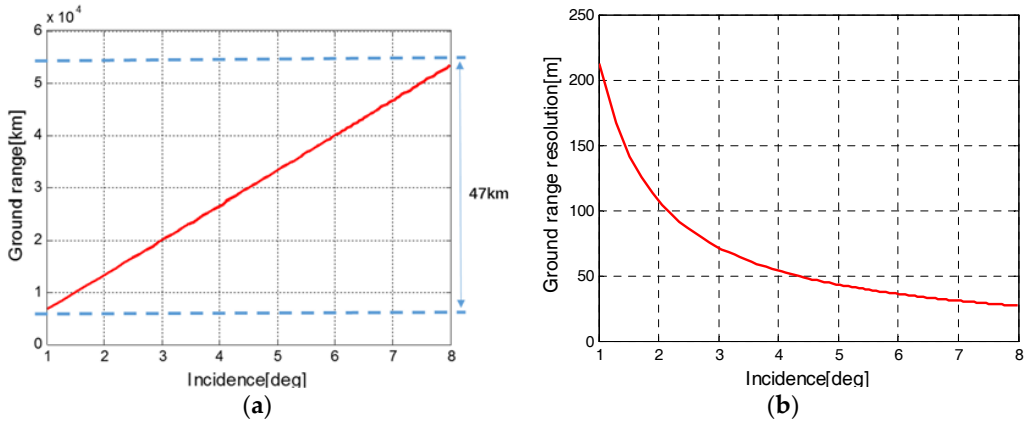

Figure 2. (**a**) Swath width and (**b**) ground-range resolution of InIRA within the incidence range.

2.2. Altimetry Principle of OST

Before the simulation of altimetric precision, we briefly introduce the OST altimetry principle. As shown in Figure 3, the baseline of InIRA is perpendicular to its orbital track, and α is the baseline tilt angle. Antenna A1 sends pulses to the ocean surface, and both of the antennas receive the reflected pulses; r_1 and r_2 are the distances between the antennas and point P, respectively. This one-transmit-two-receive working mechanism makes the effective baseline half of its physical length [10]. The received pulses of A1 and A2 are processed into two SAR complex images separately. Because of the return path difference Δr, which is caused by the existence of baseline, the corresponding phases of point P in the complex images are different. Therefore, the relationship between phase difference ϕ and return path difference Δr can be expressed by:

$$\phi = \frac{2\pi(r_2 - r_1)}{\lambda} = \frac{2\pi\Delta r}{\lambda} = \frac{2\pi B \sin(\theta - \alpha)}{\lambda} \tag{2}$$

where λ is the wavelength, B is the physical baseline length, and Δr is the return path difference, which can be approximated by the parallel component of the baseline along the look direction.

After acquiring the phase difference ϕ, with precise knowledge of r_1, the height of point P above the reference plane (could be the local mean sea level) can be deduced by:

$$h = H - r_1 \cos\theta \tag{3}$$

where H is the altitude of Tiangong II above the reference plane, r_1 is measured by timing the signal round trip delay, and θ is the incidence which is related to the phase difference ϕ.

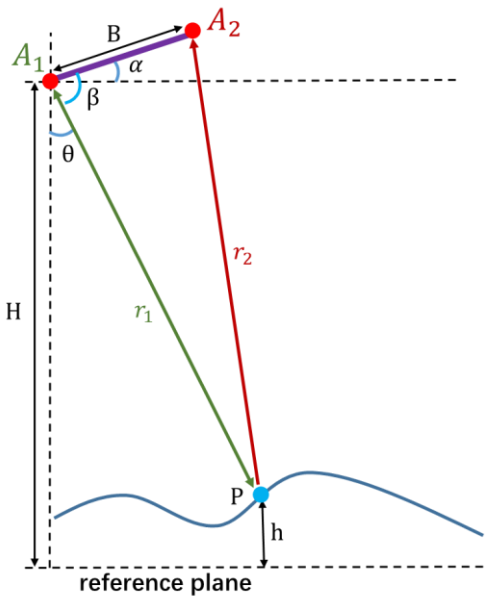

Figure 3. Ocean surface topography (OST) measurement principle (slant-range profile).

According to the geometrical relationship in Figure 3, two equations are given:

$$\cos\beta = \frac{r_1^2 + B^2 - {r_2}^2}{2r_1 B} \approx -\frac{\Delta r}{B} \tag{4}$$

$$\beta = \frac{\pi}{2} + \alpha - \theta \tag{5}$$

where β is the angle between the baseline and view direction. Combining Equations (2)–(5), the relationship between height h and phase difference ϕ is given by:

$$h = H - r_1 \cos(\frac{\pi}{2} + \alpha - \arccos(-\frac{\lambda\phi}{2\pi B})) \tag{6}$$

In fact, Equation (1) is deduced from the differential of Equation (6).

The interferometric phase ϕ_{12} which is derived from the phase difference between two SAR complex images, cannot be directly translated into ocean surface height. According to Equation (2), the return path difference Δr can be expressed by the number of wavelengths, normally Δr is longer than one wavelength. Whereas the phases recorded by complex images are confined within $[-\pi, \pi]$, this means the phases are wrapped. The relationship between unwrapped phase ϕ and interferometric phase ϕ_{12} is given in Equation (7). Phase wrapping leads to the missing of integer number n, so phase calibration must be done before acquiring the absolute ocean surface height.

$$\phi = 2\pi(\mathrm{n} + \frac{\phi_{12}}{\lambda}) \tag{7}$$

2.3. Altimetric Precision Simulation

In Equation (1), Δh can also be regarded as the relative height change above a reference sea level, $\Delta\phi$ is the corresponding phase change. Since phases are confined within $[-\pi, \pi]$, a too-large relative height change will cause phase ambiguity, also referred to as phase wrapping [10]. The altimetric

ambiguity is defined as the relative height change corresponding to a phase ambiguity of 2π. When $\Delta\phi = 2\pi$ in Equation (1), then the altimetric ambiguity is given by:

$$h_{2\pi} = \frac{\lambda r_1 \sin\theta}{B\cos(\theta - \alpha)} \tag{8}$$

Obviously, a longer baseline, smaller incidence and shorter wavelength will decrease the altimetric ambiguity or, in other words, cause the phase to be wrapped more easily by the same relative height change. Phase unwrapping is difficult, hence the altimetric ambiguity of InIRA should be large enough to avoid this problem. Figure 4a shows that the altimetric ambiguity has changed over eight times from ~64 m in the near range to ~518 m in the far range. This indicates that a relative height change larger than ~32 m in the near range will wrap the phase (since the corresponding phase is larger than π). However, phase wrapping is quite unlikely to happen, since ocean surface height variation is usually only within a few meters.

While a too-large altimetric ambiguity also brings a challenge to InIRA, for a 10-cm relative height change, the corresponding phase change is only 0.01 rad in the near range, then drops down to 0.001 rad in the far range, as shown in Figure 4b. This indicates that the phase error in the near range should be better than 0.01 rad to detect the relative height change effectively, and the phase error in the far range should be even 10 times better than in the near range. The stringent requirement on phase error demands that the system thermal noise be constrained at a certain level, and the data processing must be extremely accurate.

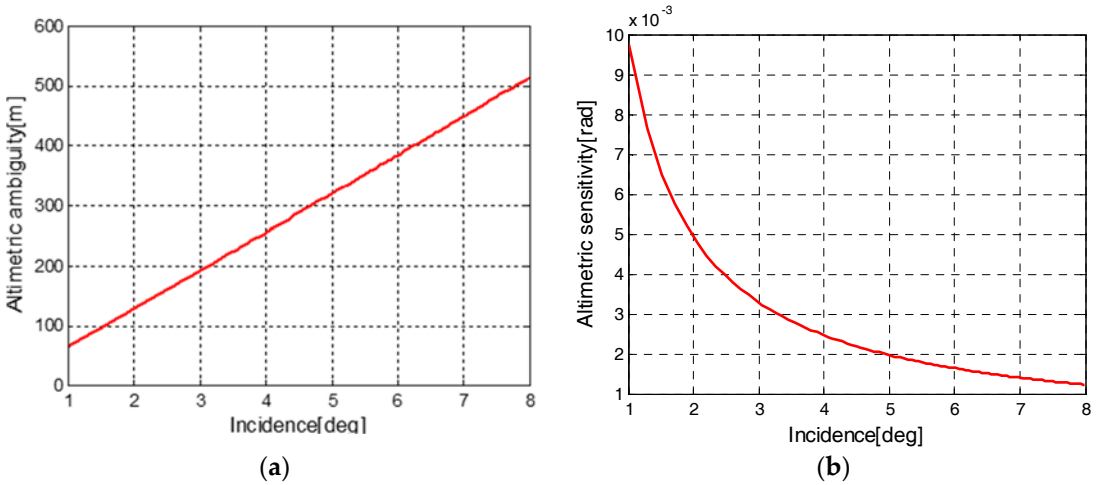

Figure 4. (**a**) Altimetric ambiguity of InIRA corresponds to a phase ambiguity of 2π; (**b**) Altimetric sensitivity of InIRA corresponds to a 10-cm ocean surface height change.

According to the analysis mentioned above, phase error will eventually determine the altimetric precision of InIRA. Phase errors are mainly from systematic errors and random errors. Systematic errors are constant or slow drifting, such as differential phase drift error or baseline roll angle error, most of which can be eliminated through calibration. In this paper we focus on the relative altimetric precision of ocean surface height, thus only random errors are considered during the simulation.

Random phase error is introduced in the simulation by multiple decorrelation factors. For any InSAR, thermal noise influences phase error the most [21], the thermal correlation factor γ_N is given by:

$$\gamma_N = \frac{SNR}{SNR + 1} \tag{9}$$

where *SNR* is the signal-to-noise ratio. Benefitting from low orbit and near-nadir incidence, the SNR of InIRA received data is very high within most of its swath, as show in Figure 5a (the SNR

curve is derived from the acquired data of InIRA), and high SNR guarantees high coherence for the interferometric data. Apart from thermal decorrelation, the presence of ocean waves will introduce a volume-scattering layer on the angle subtended by a range resolution grid, thereby introducing the volumetric decorrelation [22], which is given approximately by:

$$\gamma_v \approx e^{-2(\frac{2\pi\sigma_h B}{r_1 \lambda \tan\theta})^2} \tag{10}$$

where σ_h is the ocean surface height standard deviation, related to the significant wave height (SWH) as SWH $= 4\sigma_h$. The simulated volumetric decorrelation coefficient is shown in Figure 5b. It obviously has a much bigger influence in the near range because of the steeper incidence, and it decreases significantly as the SWH increases.

Compared to the above mentioned factors, other decorrelation factors can be neglected during the simulation [22]. The coherence of the interferometric data can be expressed by the multiplication of the decorrelation factors, as given in (11):

$$\gamma = \gamma_N \cdot \gamma_v \tag{11}$$

The coherence of InIRA acquired data is then simulated, as shown in Figure 5c, and the decrease in the far range is mainly caused by the decrease of SNR. By averaging the neighboring pixels, the phase error can be suppressed and follows the Cramer-Rao bound [21], which is given by:

$$\Delta\phi = \sqrt{\frac{1-\gamma^2}{2\gamma^2 N}} \tag{12}$$

where N is the multi-look number, γ is the coherence. Though the SNR of InIRA acquired data is very high, a large number of pixels still need to be averaged to achieve centimeter-level precision. We have simulated the altimetric precision on a 1-km grid, as shown in Figure 5d. In the near range, the precision drops due to the volumetric decorrelation. In the far range, when the incidence is above ~7.4°, the precision appears to have a steep drop, this is caused by the increase of the incidence apart from the SNR decline. As mentioned before, the altimetric precision can be increased by multi-looking, thus altimetric precision on a 1-km, 5-km and 10-km grid are simulated and compared, the SWH is set to be 2 m. As shown in Figure 5e, the precision on a 5-km grid is better than 7 cm and improves to 3 cm on a 10-km grid due to larger averaged pixel number.

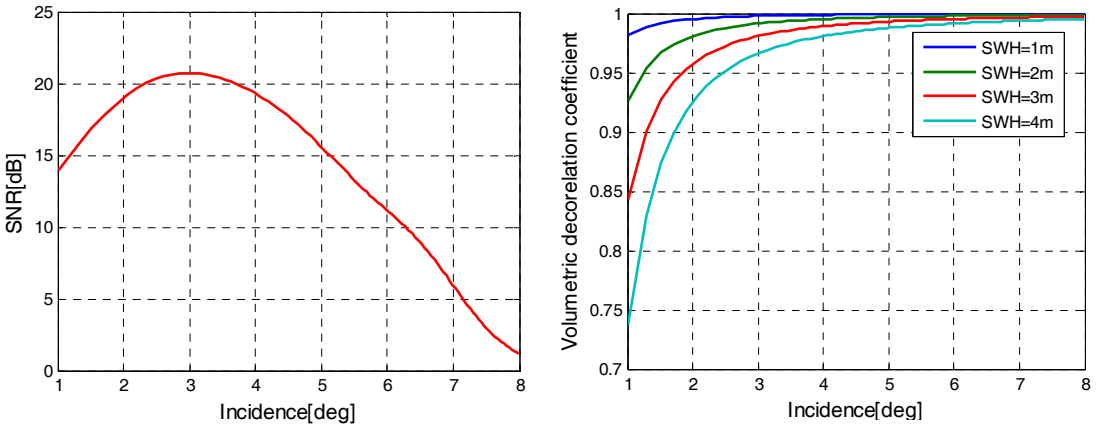

Figure 5. *Cont.*

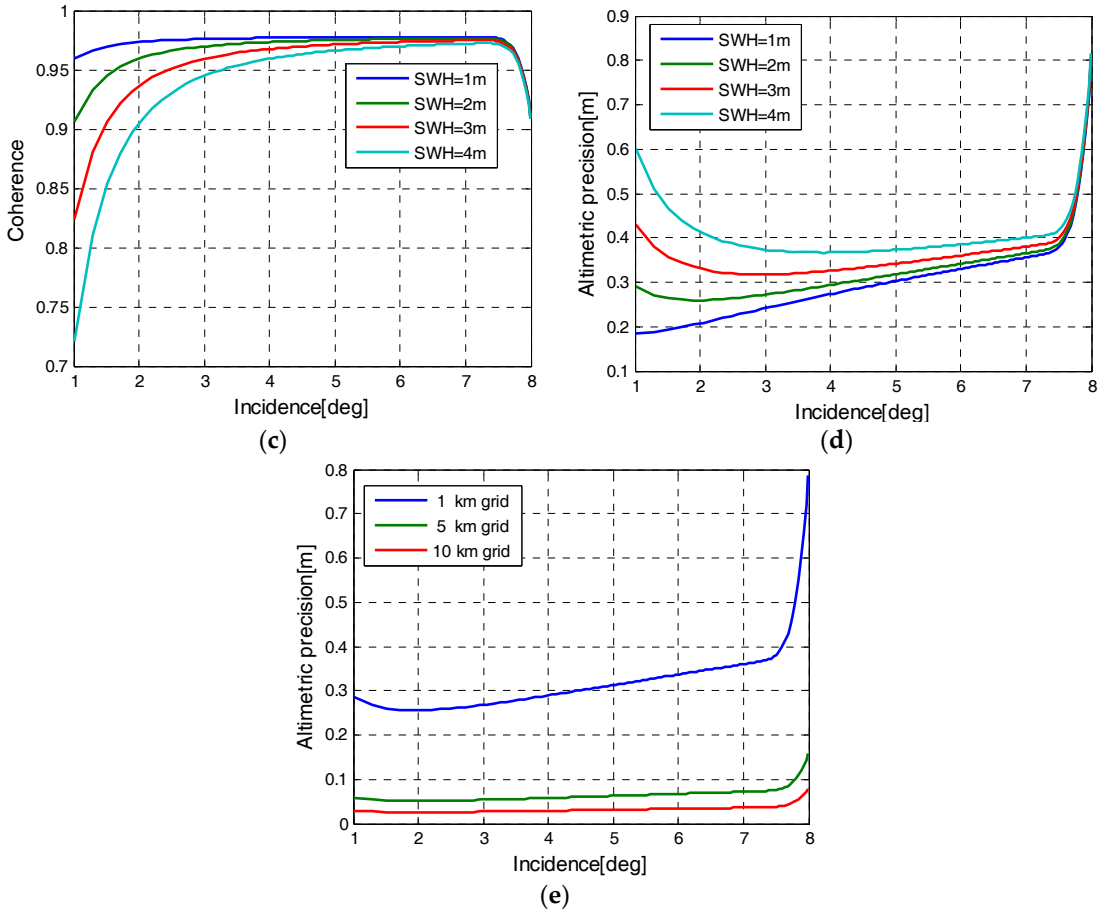

Figure 5. (**a**) Signal-to-noise ratio (SNR) curve estimated from InIRA acquired data; (**b**) volumetric decorrelation coefficient; (**c**) coherence, and; (**d**) altimetric precision under a different significant wave height (SWH) setting; (**e**) altimetric precision on a different resolution grid, the SWH is set to be 2 m during the simulation.

3. OST Altimetry Results and Analysis of InIRA

InIRA acquired the first batch of data in September 2016; the intensity image shown in Figure 6 is located in the South China Sea, next to Vietnam. The South China Sea is famous for its abundant ocean internal waves [23], and the data has just recorded this phenomenon. Some intensity discontinuity, also referred to as scalloping [24], can be seen in the far range of the ocean along the azimuth direction; this is caused by the burst working mode of InIRA. Contrary to conventional synthetic aperture radar (SAR) images, the intensity of the ocean surface in Figure 6 is much brighter than the land. The reason for this unique feature is that the received signal of InIRA contains both backscattered energy and specular-reflected energy. Compared with rough land surfaces, the signals are much easier to be specular-reflected by the ocean surface, and the specular-reflected signal takes up a much bigger proportion than the backscattered signal. In this section, the processing procedures of the interferometric data are briefly introduced, then the altimetric precision on a 1-km grid is estimated and analyzed by the processed interferometric phase.

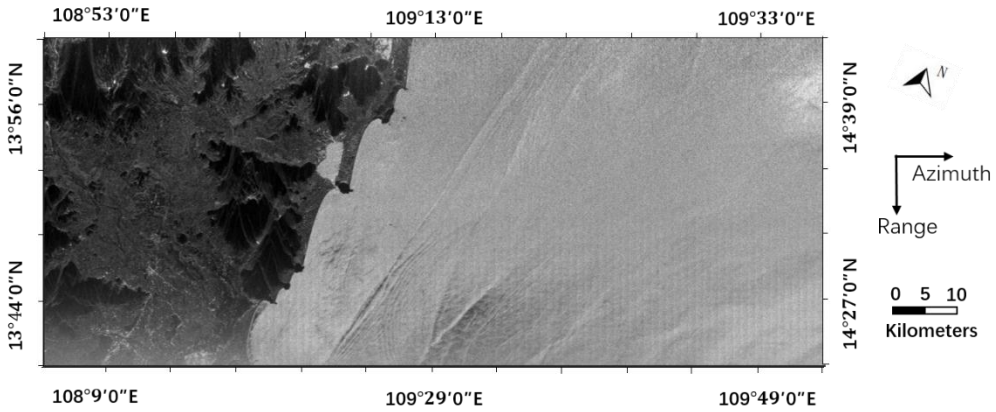

Figure 6. SAR intensity image of the South China Sea, acquired by InIRA in September 2016. The image is geocoded, the modulation of antenna pattern along the range direction is corrected. The azimuth and range directions are indicated by arrows.

3.1. Interferometric Data Processing

The interferometric data need to be coregistered, flat-earth phase removed and calibrated to finally obtain the absolute ocean surface height [10]. Though the parameter calibration of InIRA has not yet proceeded, we can still utilize the relative phase change to estimate the altimetric precision after the flat-earth phase removal.

Figure 7a is the slant-range image, under the modulation of antenna pattern, ocean surface intensity decreases rapidly in the far range, which indicates the decrease of SNR as well. Figure 7b is the coregistered phase of two SAR complex images, and fringes among the ocean area is the classic flat-earth phase. The flat-earth phase exists and changes regularly in the slant-range direction even if the topography does not change at all [10]. Among the mountainous area, the fringes seem to be distorted, which is caused by the elevation change of the mountains. Due to the decrease of SNR, phases in the far range are much noisier.

Phases in the black box in Figure 7b contains both the flat-earth phase and relative phase, which corresponds to the OST change. To acquire the relative phase, the flat-earth phase should be removed first. The flat-earth phase can be expressed by:

$$\varphi(B,\alpha,n) = \frac{2\pi B \sin(\theta-\alpha)}{\lambda} = \varphi_{fringe} + 2\pi n \tag{13}$$

where the baseline length B, baseline tilt angle α and wavelength number n need to be calibrated. φ_{fringe} is the wrapped flat-earth phase, which changes regularly along the slant-range direction, as shown in the black box in Figure 7b.

Since the relative phase change is very small according to the altimetric sensitivity simulation in Section 2.1, hence phases in the black box are mostly composed by the wrapped flat-earth phase φ_{fringe}, which contains precise information of the parameters that need to be calibrated.

Therefore, we utilize the flat-earth phase to calibrate the system parameters. Phases in the black box in Figure 7b are selected to acquire the flat-earth phase curve along the slant-range direction, then the flat-earth phase curve is fitted to the nominal Equation (13). By changing different combination of parameters (B,α,n) and seeking the minimum RMSE between flat-earth phase curve and the nominal equation. The parameters are calibrated in this way, as given in (14), and the nominal flat-earth phase is calculated and eliminated throughout the entire image. Besides, most of the systematic errors, such as differential phase drift [22], are also eliminated during this process.

$$(\hat{B},\hat{\alpha},\hat{n}) = \text{argmin}[\varphi_{fringe} - \varphi(B,\alpha,n)] \tag{14}$$

The relative phases which correspond to the topography are shown in Figure 7c. The phases vary notably among the mountainous area due to the large terrain variation. However, among the ocean area, the phases hardly change and tend to be near 0 rad. In the far range, where the internal waves exists, the phase deviates from 0 rad and looks much noisier; this phenomenon will be analyzed in Section 3.2.

Figure 7d is the coherence between two SAR complex images, and most of the ocean surface area is above 0.95. However, the coherence drops in the far range because of the decrease of SNR, especially in the internal wave area. Coherence of the mountainous area is between 0.3 and 0.7, and this relatively low coherence is mainly caused by volumetric decorrelation of the Ku-band signal, since mountains in Vietnam are covered by lush vegetation.

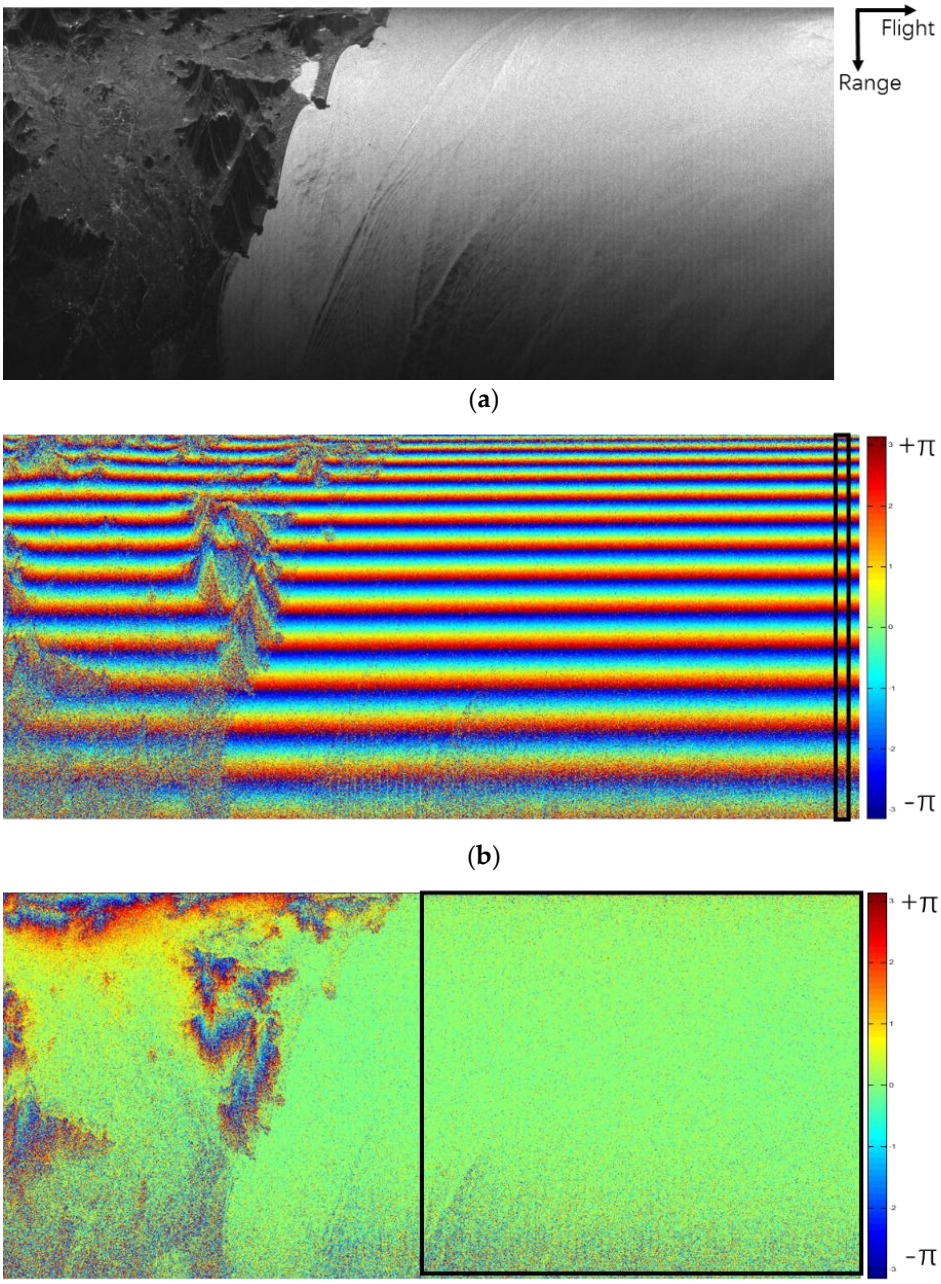

(**a**)

(**b**)

(**c**)

Figure 7. *Cont.*

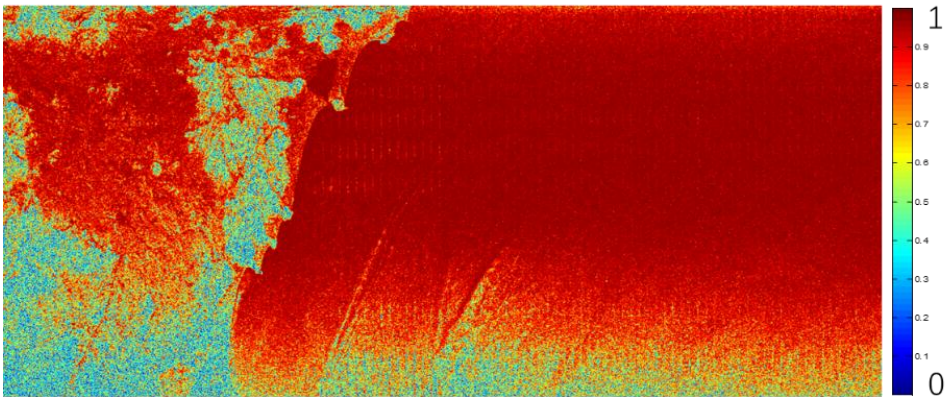

(**d**)

Figure 7. (**a**) Intensity image in slant-range direction without antenna pattern correction; (**b**) coregistered phase of two SAR complex images; (**c**) relative phase after flat-earth phase removal; (**d**) coherence between two SAR complex images. The azimuth and slant-range directions are indicated by arrows.

3.2. Altimetric Precision Estimation

According to the altimetric sensitivity analysis in Section 2.3, a 10-cm height change causes a mere 0.001~0.01 rad phase change for InIRA. The phase change is too small compared to the dynamic phase range, which is between [-π, π]. Moreover, the phase noise level is too high for OST-associated phase change to emerge on Figure 7c.

Phases in the black box in Figure 7c are multi-looked to lower the phase noise level; the phase dynamic range decreases significantly and the OST associated phases finally emerges on the 1-km grid, as shown in Figure 8.

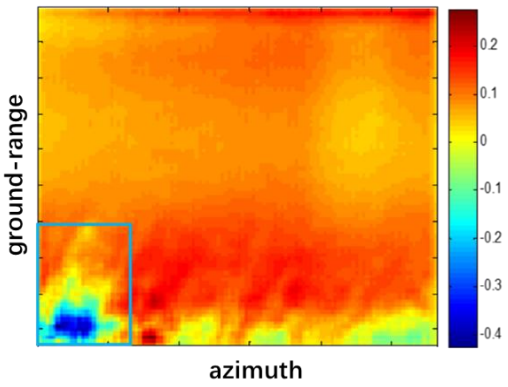

Figure 8. Multi-look interferometric phase on a 1-km grid. Phases in the blue box corresponds to the internal wave area.

The altimetric precision on a 1-km and 5-km grid are estimated by calculating the RMSE of the phase in the same ground-range bin. The simulated altimetric precision is also presented to compare with the estimated results (the SWH is set to be 1.8 m according to the meteorological data during the image acquisition), as shown in Figure 9a. Since the altimetric precision within 7°~8° incidence range is too large, the precision axis is on logarithmic scale to present the curves more clearly. Throughout the entire swath, the estimated precision on a 5-km grid (the magenta solid line) is higher than that of a 1-km grid (the red solid line) due to larger multi-look number. The estimated precision is lower than the simulated results (the dashed lines), and to analyze the reason for this difference, the precision difference curves within 1°~7° incidence range are shown in Figure 9b. Due to the random error

suppression by multi-looking, the precision difference on a 5-km grid is lower than that of a 1-km grid. However, a considerable residual difference still exits and, apart from the fact that the OST changes slightly in the area, the residual difference is mainly caused by the residual calibration error and data processing induced error. Most of these are systematic errors and cannot be further removed by multi-looking (within the 4°~5° incidence range, the difference is almost the same as the 1-km curve, which indicates that the precision difference is mainly from systematic errors).

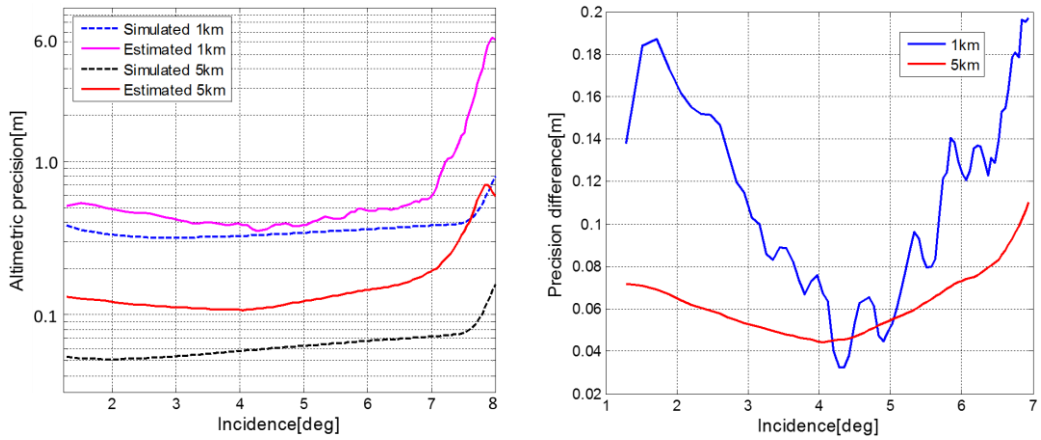

Figure 9. (**a**) Altimetric precision of the estimated and simulated results and (**b**) precision difference between the estimated and simulated results on a 1-km and 5-km grid, respectively.

In Figure 8, phases in the blue box are much lower than the surrounding phases. This anomaly causes the estimated precision drops sharply and deviates notably from the simulated precision when the incidence is above ~7°, as shown in Figure 9a. According to Figure 7a, ocean internal waves happen to exist in this area. In Figure 10, by comparing the intensity, coherence and phase images of the interval waves, we deduce that the altimetric precision decline is caused by the modulation of internal waves on ocean surface roughness. In the far range, the modulated area appears darker than the surrounding area, which indicates the decline of the SNR. As the SNR decreases, so does the coherence of the modulated area. The coherence decline increases the phase noise and worsens the altimetric precision.

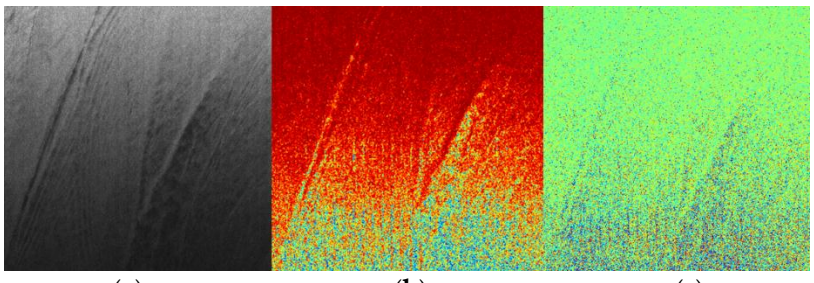

Figure 10. (**a**) Intensity (**b**) coherence and (**c**) phase image of the internal wave area.

4. Discussion

The modulation of internal waves on ocean surface roughness leads to a sharp decline in altimetric precision. However, the modulation effect seems to be quite different between the near and far range of the image. Classical SAR ocean imaging theory presumes that under 20°~60° incidence, the SAR received signal is mainly from Bragg scattering. When the modulated area gets smoother,

the backscattered signal will decrease and the internal waves will appear as dark stripes, which coincides with the situation that occurred in the far range. While different from conventional SAR, the near-nadir incidence of InIRA determines its received signals are mainly from specular reflection, so internal waves are supposed to be bright stripes, which coincides with the near range situation, and a similar phenomenon observed by satellite altimeter has also been reported in [25]. Obviously, there is an intensity boundary around ~5° incidence, as shown in Figure 11a.

The intensity boundary phenomenon also happens around the area where the ocean surface is covered by oil slick, as shown in Figure 11b. In the near range, the slicks look brighter than the surrounding area, while darker in the far range. Since the modulation of oil slick also makes the ocean surface smoother, so the intensity boundary can be explained by the same reason as of the internal waves'.

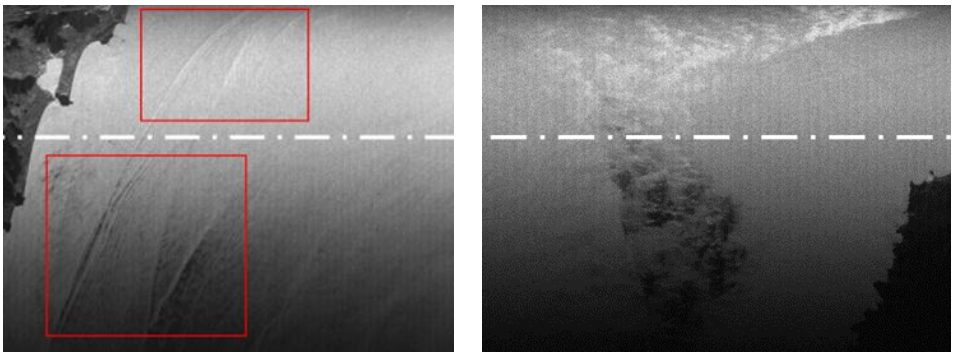

(**a**) (**b**)

Figure 11. Intensity boundary phenomenon of (**a**) internal waves (as shown in the red boxes); (**b**) oil slick.

Considering the near-nadir incidence of InIRA, the intensity boundary can be explained as follows.

In the near range, the incidence is almost vertical, meanwhile, a small surface slope induced by ocean waves also exists, as shown in Figure 12. When radar signals illuminate the ocean surface, most of the signals will reflect straight back into the receiver. Since under the modulation of internal waves or oil slick, the ocean surface get smoother, so reflected signals from modulated ocean area become stronger. This makes the internal waves or oil slick appear brighter than the surrounding area.

In the far range, the incidence increases, however, the surface slope does not increase since it is largely dominated by the local sea state. Though most of the radar signals are also specular-reflected, only few of them can head back into the receiver. It gets even worse around the modulated area since the backscattered signal also decreases because of the smoother surface roughness. This makes the internal waves or oil slick appear darker than the surrounding area.

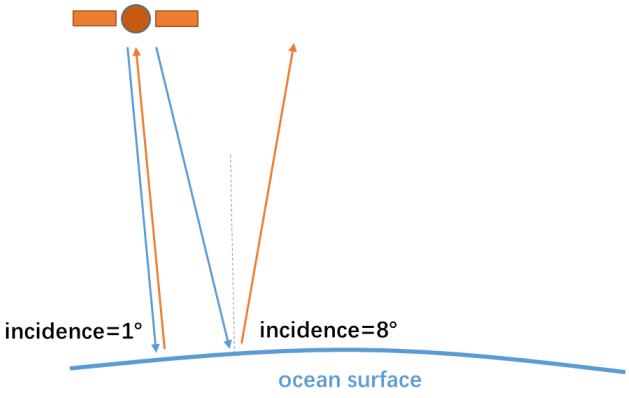

Figure 12. Schematic diagram of the intensity boundary phenomenon.

The position where the intensity boundary locates is determined by ocean wave slope, and the ocean wave slope is dominated by the local sea state. So future near-nadir InSAR should consider this phenomenon while designing the incidence range. Our future work will derive the relationship between the intensity boundary and sea state from the statistics of the acquired data.

5. Conclusions

As an experimental payload, even though some of the system parameters are limited by the current technique, InIRA has shown its great potential in measuring the OST with high precision that have never been resolved before. Based on the performance analysis of InIRA in this paper, here are some suggestions on parameter design for the future near-nadir InSAR.

(1) According to the intensity boundary phenomenon, the available swath of high altimetric precision will be narrower than expected. As for InIRA, when the incidence range is 1°~5°, the swath will decrease to only 20 km. This narrow swath can hardly fulfill the altimetry on sub-mesoscale oceanic processes. Therefore, future near-nadir InSAR could fly on a higher orbit to increase the swath width.

(2) Flying on a higher orbit means the SNR of the received signal will decrease significantly, thereby definitely increasing the phase noise level. As mentioned before, multi-looking is one of the most effective ways to lower the phase noise, and the 3-cm altimetric precision on a 10-km grid is much higher than that of a 1-km grid, according to the simulation. However, it is quite challenging for the 10-km grid to resolve mesoscale or sub-mesoscale oceanic processes whose physical dimension is only about 15~300 km. Therefore, future near-nadir InSAR should guarantee an even higher intrinsic image resolution so that a larger multi-look number could be acquired on the same grid.

(3) Baseline length is the key parameter which guarantees high altimetric precision for near-nadir InSAR. Meanwhile, a longer baseline will mitigate the stringent requirement for a systematic phase noise level and data processing precision, allowing the near-nadir InSAR to achieve better performance much more easily.

Acknowledgments: The authors would like to thank the Key Laboratory of Space Utilization, Technology and Engineering Center for Space Utilization, Chinese Academy of Sciences for providing the InIRA data. The authors would also like to thank the anonymous reviewers and the editors for their comments and suggestions that improved the manuscript.

Author Contributions: Weiya Kong conceived and performed the experiments; Jinsong Chong and Weiya Kong designed the research and contributed to the article's organization; Hong Tan provided the data for comparative analysis. Weiya Kong drafted the manuscript, which was revised by all authors. All authors read and approved the final manuscript.

Conflicts of Interest: The authors declare no conflict of interest.

References

1. Pitz, I.; Otto, A.; Schmidt, M. Ocean surface topography constellation: The next 15 years in satellite altimetry. *Kybern. Praha* **2010**, *2*, 490–493.
2. Coleman, R. Satellite altimetry and earth sciences: A handbook of techniques and applications. *Eos Trans. Am. Geophys. Union* **2013**, *82*, 376. [CrossRef]
3. Zawadzki, L.; Ablain, M. Accuracy of the mean sea level continuous record with future altimetric missions: Jason-3 vs. Sentinel-3a. *Ocean Sci. Discuss.* **2016**, *12*, 1511–1536. [CrossRef]
4. Fu, L.L.; Stammer, D.; Leben, R.R.; Chelton, D.B. Improved spatial resolution of ocean surface topography from the t/p-jason-1 altimeter mission. *Eos Trans. Am. Geophys. Union* **2003**, *84*, 241–248. [CrossRef]
5. Fu, L.L.; Alsdorf, D.; Morrow, R.; Rodriguez, E.; Mognard, N. *Swot: The Surface Water and Ocean Topography Mission: Wide-Swath Altimetric Elevation on Earth*; Jet Propulsion Lab: Pasadena, CA, USA, 2012.
6. Fu, L.L.; Ferrari, R. Observing oceanic submesoscale processes from space. *Eos Trans. Am. Geophys. Union* **2008**, *89*, 488. [CrossRef]

7. Kim, S.Y. Observations of submesoscale eddies using high-frequency radar-derived kinematic and dynamic quantities. *Cont. Shelf Res.* **2010**, *30*, 1639–1655. [CrossRef]
8. Rodriguez, E.; Morris, C.S.; Belz, E.J. A global assessment of srtm performance. *Photogramm. Eng. Remote Sens.* **2006**, *72*, 249–260. [CrossRef]
9. Ulander, L.M.H.; Askne, J. Repeat-pass sar interferometry over forested terrain. *IEEE Trans. Geosci. Remote Sens.* **1995**, *33*, 331–340.
10. Rodriguez, E.; Martin, J.M. Theory and design of interferometric synthetic aperture radars. *Radar Signal Process. IEE Proc.* **1992**, *39*, 147–159. [CrossRef]
11. Musa, Z.N.; Popescu, I.; Mynett, A. A review of applications of satellite sar, optical, altimetry and dem data for surface water modelling, mapping and parameter estimation. *Hydrol. Earth Syst. Sci. Discuss.* **2015**, *12*, 4857–4878. [CrossRef]
12. Fu, L.L.; Rodriguez, E. Wide-swath altimetric measurement of ocean surface topography. In Proceedings of the 2003 International Union of Geodesy and Geophysics (IUGG) Conference, Sapporo, Japan, 30 June–11 July 2003.
13. Pollard, B.D.; Rodriguez, E.; Veilleux, L.; Akins, T.; Brown, P.; Kitiyakara, A.; Zawadski, M.; Datthanasombat, S.; Prata, A. The Wide Swath Ocean Altimeter: Radar Interferometry for Global Ocean Mapping with Centimetric Accuracy. In Proceedings of the IEEE Aerospace Conference, Big Sky, MT, USA, 9–16 March 2002; Volume 1002, pp. 1007–1020.
14. Fjørtoft, R.; Gaudin, J.M.; Pourthie, N.; Lion, C. Karin—The ka-band radar interferometer on swot: Measurement principle, processing and data specificities. In Proceedings of the IEEE International Geoscience and Remote Sensing Symposium, Honolulu, HI, USA, 25–30 July 2010; pp. 4823–4826.
15. Wu, X.; Hensley, S.; Rodriguez, E.; Moller, D.; Muellerschoen, R.; Michel, T. Near nadir ka-band sar interferometry: Swot airborne experiment. In Proceedings of the Geoscience and Remote Sensing Symposium, Vancouver, BC, Canada, 24–29 July 2011; pp. 2681–2684.
16. Fjortoft, R.; Gaudin, J.M.; Pourthie, N.; Lalaurie, J.C.; Mallet, A.; Nouvel, J.F.; Martinot-Lagarde, J.; Oriot, H.; Borderies, P.; Ruiz, C. Karin on swot: Characteristics of near-nadir ka-band interferometric sar imagery. *IEEE Trans. Geosci. Remote Sens.* **2014**, *52*, 2172–2185. [CrossRef]
17. Altenau, E.H.; Pavelsky, T.M.; Moller, D.; Lion, C.; Pitcher, L.H.; Allen, G.H.; Bates, P.D.; Calmant, S.; Durand, M.; Smith, L.C. Airswot measurements of river water surface elevation and slope: Tanana River, AK. *Geophys. Res. Lett.* **2017**, *44*, 181–189. [CrossRef]
18. Jackson, C. *Synthetic Aperture Radar Marine User's Manual*; U.S. Department of Commerce: Washington, DC, USA, 2004; pp. 279–360.
19. Doerry, W.A. Atmospheric attenuation and sar operating frequency selection. In Proceedings of the Workshop on Synthetic Aperture Radar Technology, Huntsville, AL, USA, 22–23 October 2003.
20. Lee, J.S.; Hoppel, K.W.; Mango, S.A.; Miller, A.R. Intensity and phase statistics of multilook polarimetric and interferometric sar imagery. *IEEE Trans. Geosci. Remote Sens.* **1994**, *32*, 1017–1028.
21. Just, D.; Bamler, R. Phase statistics of interferograms with applications to synthetic aperture radar. *Appl. Opt.* **1994**, *33*, 4361–4368. [CrossRef] [PubMed]
22. Esteban Fernandez, D.; Pollard, B.; Vaze, P.; Abelson, R. Swot Project Mission Performance and Error Budget. Available online: https://swot.oceansciences.org/documents.htm (accessed on 8 September 2017).
23. Duda, T.F.; Lynch, J.F.; Irish, J.D.; Beardsley, R.C.; Ramp, S.R.; Chiu, C.S.; Tang, T.Y.; Yang, Y.J. Internal tide and nonlinear internal wave behavior at the continental slope in the northern south china sea. *IEEE J. Ocean. Eng.* **2004**, *29*, 1105–1130. [CrossRef]
24. Holzner, J.; Bamler, R. Burst-mode and scansar interferometry. *IEEE Trans. Geosci. Remote Sens.* **2002**, *40*, 1917–1934. [CrossRef]
25. Magalhaes, J.M.; Silva, J.C.B.D. Satellite altimetry observations of large-scale internal solitary waves. *IEEE Geosci. Remote Sens. Lett.* **2017**, *14*, 534–538. [CrossRef]